Cite this: *Dalton Trans.*, 2021, **50**, 3369

Ligand symmetry significantly affects spin crossover behaviour in isomeric [Fe(pybox)₂]²⁺ complexes†

Run-Guo Wang,^a Yin-Shan Meng,^b Fang-Fang Gao,^c Wan-Qing Gao,^a Chun-Hua Liu,^a Anyang Li,^b Tao Liu^{*b} and Yuan-Yuan Zhu^{*a,b}

The understanding of the correlation between the spin-state behaviour and the structural features in transition-metal complexes is of pronounced importance to the design of spin crossover compounds with high performance. However, the study of the influence of ligand symmetry on the spin crossover properties is still limited due to the shortage of suitable structural systems. Herein we report the magneto-structural correlations of three mononuclear Fe(II) isomers with respect to their ligand symmetry. In this work, two phenyl-substituted *meso* and *optically pure* pybox ligands were employed to construct *meso* (**1**), *optically pure* (**2**), and *racemic* (**3**) ligand types of [Fe(pybox)₂]²⁺ complexes. Their magnetic susceptibilities were measured *via* temperature-dependent paramagnetic ¹H NMR spectroscopy. We fitted the midpoint temperatures of the transition ($T_{1/2}$) of 260 K for **1**(ClO₄), 247 K for **2**(ClO₄), and 281 K for **3**(ClO₄). The influence of structural symmetry on spin crossover was rationalized through density functional theory calculations. The optimized structures of [Fe(pybox)₂]²⁺ complex cations show that the geometric distortion of the central FeN₆ coordination sphere is mainly caused by the steric congestions between adjacent phenyl substituents. In these compounds, there is a distinct correlation that more steric congestions produce larger coordination distortion and favor the electron configuration in the high-spin state, which reflects in the increase of $T_{1/2}$. Additionally, the influence of the counter anion and lattice solvent on the *meso* series compounds was inspected. It is revealed that multiple factors dominate the spin-state behaviour in the solid state. This work provides deep insight into the effect of ligand symmetry on the spin transition behaviour in spin crossover compounds. It demonstrates that molecular symmetry should be considered in the design of spin crossover compounds.

Received 20th November 2020,

Accepted 27th January 2021

DOI: 10.1039/d0dt03978k

rsc.li/dalton

Introduction

The development of spin crossover (SCO) transition metal complexes has been widely recognized as a promising approach for constructing bistable magnetic materials at the single-molecule level.^{1,2} The SCO phenomenon exists in some

complexes bearing d^{4–7} transition metals to which organic ligands with suitable ligand field strength are coordinated.³ In these complexes, the electronic configuration of the central metal involves the reversible rearrangement between high-spin (HS) and low-spin (LS) states under physical stimuli such as temperature, pressure, light, solvent, magnetic field, *etc.* The consequence of the change in the count of unpaired electrons can switch the magnetic moment directly and influence other physical properties including the dielectric constant, electrical resistance, and crystallographic phase. The rearrangement of the electron configuration in the d orbital is triggered by the relative energy magnitude of ligand field splitting between the t_{2g} and e_g molecular orbitals (Δ) and pairing energy of electrons (P). When $\Delta > P$, pairing of electrons is favoured. When $\Delta < P$, electrons tend to separately locate in maximum d orbitals. Due to the splitting energy, Δ is sensitive with respect to the ligand field strength, so an appropriate coordination environment plays a vital role in the occurrence of SCO in a measurable temperature range. The fine-tuning of the ligand field

^aSchool of Chemistry and Chemical Engineering, Anhui Key Laboratory of Advanced Catalytic Materials and Reaction Engineering, Hefei University of Technology, Hefei 230009, China. E-mail: yyzhu@hfut.edu.cn

^bState Key Laboratory of Fine Chemicals, Dalian University of Technology, 2 Linggong Road, Dalian 116024, China. E-mail: liutao@dlut.edu.cn

^cKey Laboratory of Synthetic and Natural Functional Molecule of Ministry of Education, College of Chemistry and Materials Science, Northwest University, Xi'an, 710127, P. R. China. E-mail: liay@nwu.edu.cn

† Electronic supplementary information (ESI) available: Synthesis, characterization, and NMR spectra of complexes, X-ray single crystal structures, PXRD pattern, and structural analysis of complexes and supplementary magnetic data. CCDC 2045167–2045172. For ESI and crystallographic data in CIF or other electronic format see DOI: 10.1039/d0dt03978k

may affect SCO behaviour to a large extent. Extensive research on SCO complexes shows that the ligand's substituent, counterion, co-crystallized solvent, and polymorphism in the solid state are operative factors to influence their spin-state properties.⁴ Very recently, chirality in enantiopure ligands that could influence SCO was investigated in some mononuclear complexes and coordination polymers.^{5–8} For example, the enantiopure and racemic isomers are crystallized in chiral and achiral space groups, respectively. The discriminations in the molecular structure and packing probably change their ligand field in which the tunable SCO properties can be attained.

Tridentate pincer-type *ter*-imine molecules constitute a large family of organic ligands in constructing SCO-active compounds.⁹ We first demonstrated that a new type of tridentate nitrogen ligand, pyridine-2,6-bis(oxazoline) (pybox), is efficient in constructing an SCO-active mononuclear complex.¹⁰ Subsequently, the tuning of SCO properties *via* the ligand structure, counter anion, and co-crystallized solvent was studied by us and other groups.^{11–13} Considering that some pybox ligands contain a chiral centre, [Fe(pybox)₂]²⁺ type complexes are an ideal platform to evaluate the possible correlation between chirality and SCO behaviour. More recently, the Halcrow group and we independently discovered the subtle structural diversity of homogeneous and heterogeneous [Fe(pybox)₂]²⁺ complexes, in which two same enantiopure ligands and a pair of racemic ligands are assembled into the complexes, respectively, resulting in significantly different spin-state behaviours.^{14,15} In comparison with heterogeneous compounds, their homogeneous analogues have lower symmetry both in the molecular structure and the crystallized space group. The reduced molecular symmetry produces structural distortion of the coordination sphere of the metal ion and ultimately affects the spin-state behaviour.¹⁶ To further explore the influence of ligand symmetry in isomers, we thought to investigate and compare the spin-state behaviour of [Fe(pybox)₂]²⁺ complexes when the ligand's chirality is in the *optically pure*, *racemic* and *meso* forms. This research will deepen the understanding of SCO behaviour in transition metal complexes when the ligands contain a chiral element. In this contribution, the phenyl-substituent *meso* type pybox ligand (**L^{meso}**) is synthesized for the first time. Using **L^{meso}** as the ligand, the Fe(II) mononuclear complexes bearing four different counter anions (ClO₄⁻, BF₄⁻, PF₆⁻, and BPh₄⁻) are obtained. We investigated their temperature-dependent mag-

netic properties in solution and in the solid state. Compared with their enantiopure and racemic analogues, the diverse SCO behaviour caused by the variation in chirality in the pybox ligand is observed. Density Functional Theory (DFT) calculations are carried out to optimize the geometries of three forms of [Fe(pybox)₂]²⁺ complex cations. The calculated results are rationalized with the experimental magnetic and structural data. Furthermore, the magneto-structural correlation is discussed.

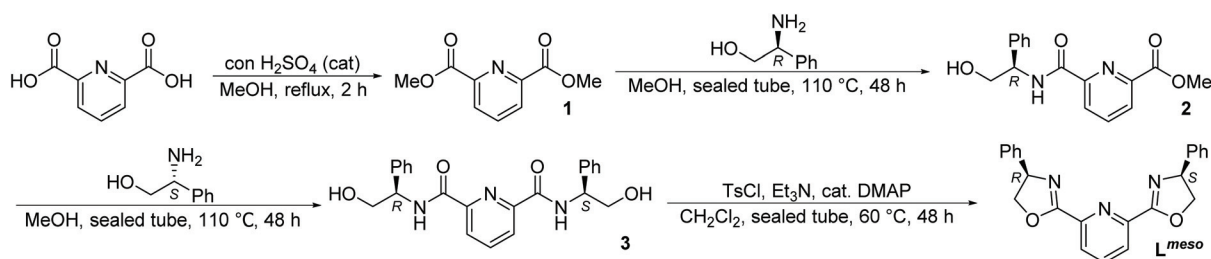
Results and discussion

Synthesis of the ligand

In this work, the *meso* type pybox ligand (**L^{meso}**) was synthesized for the first time. The detailed synthetic procedure is shown in Scheme 1. First, amidation of dimethyl pyridine-2,6-dicarboxylate with (*R*)- and (*S*)-phenylglycinol stepwise generated **3** with a moderate yield. Then the formation of two oxazoline rings bearing opposite chiral centres through intramolecular cyclization afforded **L^{meso}** in a high yield. The structure and purity of **L^{meso}** were confirmed by ¹H and ¹³C NMR, mass spectroscopy, and elemental analysis. **L^{meso}** and its *optically pure* analogue (**L^{R/S}**) possess totally different molecular symmetries. In the *optically pure* form **L^{R/S}**, there exists one C₂ rotation axis. The overall symmetry of **L^{R/S}** is of the point group C₂; so this molecule shows optical activity. Nevertheless, **L^{meso}** belongs to the C_s point group. A symmetry mirror (σ) divides the molecule equally, making **L^{meso}** an achiral molecule (see Fig. 1(a)).

Synthesis and characterization of the complexes

The synthetic procedure of **L^{meso}** series complexes bearing different counter anions is as follows. Treatment of 1 equiv. of iron(II) salt with 2 equiv. of **L^{meso}** in methanol afforded the following complexes as dark red-coloured precipitates: [Fe(**L^{meso}**)₂][ClO₄]₂ (**1(ClO₄)**), [Fe(**L^{meso}**)₂][BF₄]₂ (**1(BF₄)**), [Fe(**L^{meso}**)₂][PF₆]₂ (**1(PF₆)**), and [Fe(**L^{meso}**)₂][BPh₄]₂ (**1(BPh₄)**). Then the crystals of the four complexes suitable for single X-ray diffraction analysis were obtained through recrystallization. The detailed operation was carried out *via* slow gas evaporation of diethyl ether into the diluted acetonitrile solution of complexes. All crystals show dark red colour. Among them, **1(ClO₄)** is a solvent-free crystal while the other three contain a lattice



Scheme 1 The synthetic route of ligand **L^{meso}**.

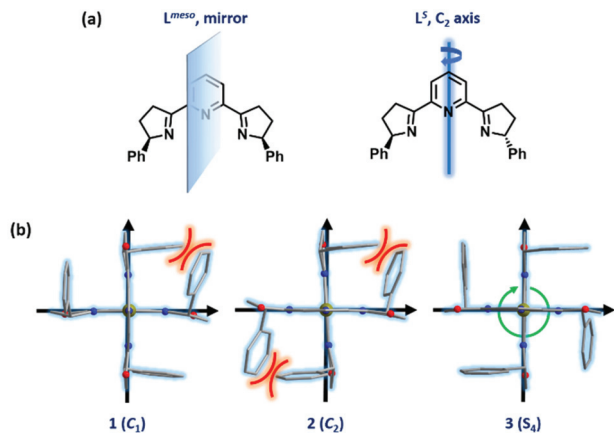


Fig. 1 The structures of ligands (a) L^{meso} and L^S . (b) The structures of complex cations in $1(ClO_4)$ (left), $2(ClO_4)$ (middle) and $3(ClO_4)$ (right).

solvent. The sums of acetonitrile per complex are included in their names. For comparison of the structural and magnetic discrimination imposed by ligand symmetry, the homochiral complex $[Fe(L^S)_2][ClO_4]_2$ ($2(ClO_4)$) and the heterochiral complex $[Fe(L^R)(L^S)][ClO_4]_2$ ($3(ClO_4)$) were synthesized. Their structures and purity were confirmed through single crystal X-ray diffraction analysis (see Fig. S19–S30[†]) and paramagnetic 1H NMR spectroscopy (see Fig. S6–S9[†]). The phase purity of bulk samples was determined through powder XRD analysis (see Fig. S37–S42[†]). In addition, the content of the lattice solvent was further determined by elemental analysis and TGA measurement (see Fig. S31–S36[†]).

Single crystal X-ray diffraction analyses revealed that four complexes $1(ClO_4)$, $1(BF_4) \cdot MeCN$, $1(PF_6) \cdot MeCN$, and $1(BPh_4) \cdot MeCN \cdot Et_2O$ adopt the achiral space group $C2/c$, $Pbca$, $C2/c$, and $P2_1/n$, respectively (see Fig. S19–S30[†]). Their octahedra of Fe(II) centres vary in geometric distortion due to the influence of the anion and lattice solvent in some cases (see Fig. S3[†]). A large anion and lattice solvent tend to cause great distortion and thus favour a HS state. Two control complexes $2(ClO_4) \cdot MeOH$ and $3(ClO_4) \cdot MeOH$, which were grown from liquid–liquid diffusion in methanol, crystallized in the chiral space group $P2_12_12_1$ and the achiral space group $P2_1/n$, respectively.

For a comparison of the X-ray structures in the solid state, their structural diversity caused by ligand symmetry was investigated in three perchlorate series complexes. The crystal structures of complex cations in $1(ClO_4)$, $2(ClO_4)$ and $3(ClO_4)$ are shown in Fig. 1(b). First, they possess different structural symmetries. The approximate molecular point groups of complex cations are C_1 for $1(ClO_4)$, C_2 for $2(ClO_4)$, and S_4 for $3(ClO_4)$. Among them, only $2(ClO_4)$ displays optical activity. In $3(ClO_4)$, a pair of *racemic* ligands are coordinated to the central Fe(II) cation; so it is actually a *meso* type complex. Second, the positions of phenyl substituents are variable with respect to the chirality of ligands in the complex. In these phenyl substituent complexes, the intramolecular π – π stackings between phenyl and pyridine rings are thought to stabilize the complex structure.^{14,15,17} There exist

intramolecular steric congestions between phenyl substituents in $1(ClO_4)$ and $2(ClO_4)$, causing the deviation of coplanarity between two oxazoline rings and the central pyridine ring (see Fig. 1(b)). In contrast, four phenyl substituents in $3(ClO_4)$ are separately located at different positions. Each pair of phenyl substituents is ‘perfectly’ parallel to the pyridine ring from the other ligand. The sums of the steric phenyl pair are one in $1(ClO_4)$, two in $2(ClO_4)$ and null in $3(ClO_4)$. The steric congestion has a great impact on the molecular structure that not only affects the π – π stackings between phenyl and pyridine rings but also causes the distortion of the oxazoline ring (see Fig. 1(b)).

The symmetry discrimination of the three complexes in solution was investigated *via* 1H NMR spectroscopy. The 1H NMR spectra of three Fe(II) complexes and isostructural Zn(II) complexes (perchlorate as the counter anion) are shown in Fig. S14[†] and Fig. 2. Although the 1H NMR spectra of L^{meso} and $L^{S/R}$ are similar (see Fig. S13[†]), the proton signals in three Fe(II) series complexes and their diamagnetic Zn(II) analogues exhibit significant differences both in the chemical shift and in sum of peaks (see Fig. S14[†] and Fig. 2). 1H NMR spectra reveal that the *meso* ligand type $1(ClO_4)$ -Zn shows the lowest symmetry. The doubling proton peaks in the phenyl ring range is observed compared with its *optically pure* and *racemic* forms due to two phenyl substituents in one ligand being inequivalent in the chemical environment (see Fig. 2). A similar phenomenon occurs in their pyridine and oxazoline proton ranges. It is evident that the differently arranged types of phenyl rings can considerably change the electronic state and thus affect their ligand field.

Solution-state magnetic studies

The geometric coordination and SCO behaviour of complexes in the solid state are greatly affected by intermolecular cooperativity, lattice solvent, and crystal packing. Therefore, it is inaccurate to inspect the unique influence of the ligand structure on their SCO properties through magnetic measurement in the solid state. Nevertheless, the complex molecules in solution are well isolated by the solvent; so such effects can be

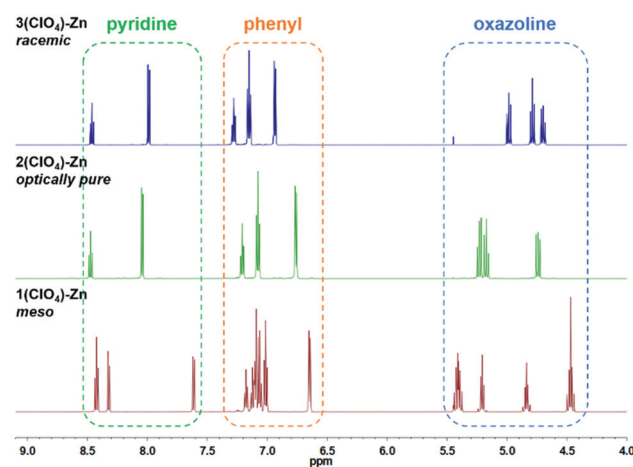


Fig. 2 The merged 1H NMR spectra of $1(ClO_4)$ -Zn, $2(ClO_4)$ -Zn, and $3(ClO_4)$ -Zn in CD_3CN at 298 K.

excluded to a great extent. It is widely accepted that the paramagnetic ^1H NMR spectroscopy method is reliable to measure the temperature-dependent magnetic susceptibilities in solution.^{18–20} Hence, the temperature-dependent magnetic susceptibilities of three complexes, $1(\text{ClO}_4)$, $2(\text{ClO}_4)$, and $3(\text{ClO}_4)$, were measured in CD_3CN via paramagnetic ^1H NMR spectroscopy. As shown in Fig. S15a, S16a and S17a,† their NMR proton signals all exhibit a considerable chemical shift towards downfield in accordance with the increase in temperature, causing a gradual rise of the HS state fraction. The $\chi_{\text{M}}T$ values at specific temperatures were calculated using the Evans method²¹ (see eqn (1)):

$$\chi_{\text{M}}T = \left(\frac{3\Delta f}{4mf} + \chi_{\text{M}}^{\text{dia}} \right) \times T \quad (1)$$

where m is the concentration of the paramagnetic solution in g mL^{-1} , f is the spectrometer frequency in Hz, Δf is the shift of the CD_3CN peak in the paramagnetic solution compared to pure CD_3CN in Hz (see Fig. S15b, S16b and S17b†), and $\chi_{\text{M}}^{\text{dia}} = 0.5 \text{ M} \times 10^{-6} \text{ cm}^3 \text{ mol}^{-1}$ (M is the molecular weight).²² The calculated data were plotted in the $\chi_{\text{M}}T$ vs. T form, which indicated that the three complexes all underwent gradual SCO within the measured temperature range, from 243 to 333 K. These detached $\chi_{\text{M}}T$ plots were modeled as a gradual and complete SCO curve using the following regular solution model (eqn (2)). This fitting can derive some thermodynamic parameters in the SCO process:^{23,24}

$$\chi_{\text{M}}T = \frac{\chi_{\text{M}}T_{(\text{max})}}{1 + e^{\left(\frac{\Delta H}{RT} - \frac{\Delta S}{R} \right)}} \quad (2)$$

where $\chi_{\text{M}}T_{(\text{max})}$ is the maximum $\chi_{\text{M}}T$ value for the complete HS state. As per our previous experience with this family of complexes, the saturated $\chi_{\text{M}}T$ value of $3.9 \text{ cm}^3 \text{ K mol}^{-1}$ was used in eqn (2) (Fig. 3).

For the data of the three complexes, good fitting with the least squares value larger than 0.98 was obtained and the thermodynamic parameters, ΔH , ΔS , and $T_{1/2}$, were fitted (see Table 1). Our fitting results for $2(\text{ClO}_4)$ and $3(\text{ClO}_4)$ are consistent with the results reported by the Halcrow group.¹⁴ The SCO midpoint temperatures ($T_{1/2}$) of the three complexes in CD_3CN follow the order of $3(\text{ClO}_4) > 1(\text{ClO}_4) > 2(\text{ClO}_4)$, suggesting that *racemic* ligands in the complex impose a stronger ligand field than the other two forms. The lowest $T_{1/2}$ of $2(\text{ClO}_4)$ reveals that two homochiral ligands provide the weakest ligand field, which is probably caused by the geometric distortion of the coordination sphere due to two steric congestions of the phenyl substituents in the structure.

Theoretical studies

To rationalize the varied SCO behaviour and structural stability for the three types of complexes, three complex cations (1–3) were optimized at the M06/6-31G(d) level^{25,26} in two spin multiplicities, high spin ($S = 2$) and low spin ($S = 0$). The optimized structures in the singlet and quintet states are shown in Fig. 4 and S47.†

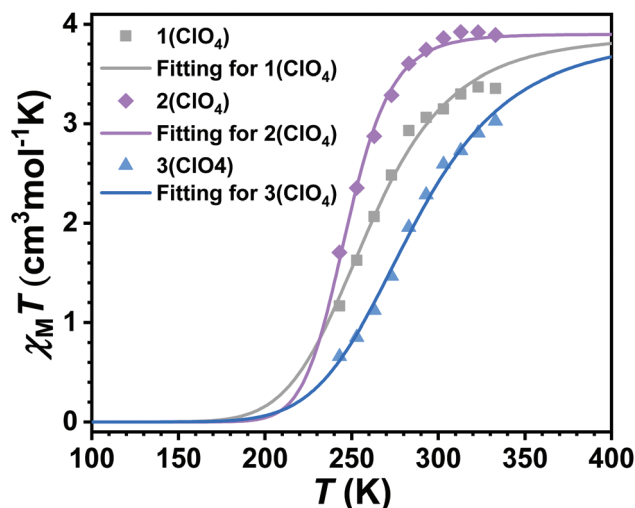


Fig. 3 Temperature dependence of $\chi_{\text{M}}T$ for $1(\text{ClO}_4)$, $2(\text{ClO}_4)$, and $3(\text{ClO}_4)$ in CD_3CN . The plots represent the experimental data which were collected between 243 and 333 K with an interval of 10 K. The lines correspond to the best fit found for each compound using the regular solution model.

Table 1 Solution-state thermodynamic parameters in SCO for the three complexes

No	$T_{1/2}$ ^a (K)	ΔH (kJ mol^{-1})	ΔS ($\text{J mol}^{-1} \text{ K}$)	LS^b
$1(\text{ClO}_4)$	260	22.8	88	0.9812
$2(\text{ClO}_4)$	247	22.4	76	0.9931
$3(\text{ClO}_4)$	281	23.3	83	0.9944

^a $T_{1/2} = \Delta H/\Delta S$. ^b Least squares.

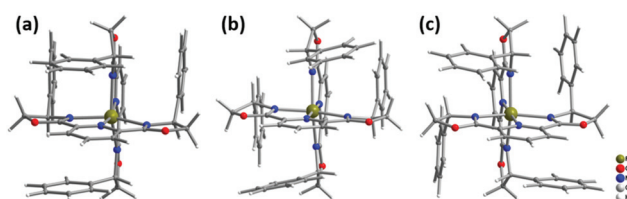


Fig. 4 The optimized quintet structures of (a) 1, (b) 2, and (c) 3.

Some key structural parameters derived from the optimized structures which can quantitatively reflect the geometric distortion of the FeN_6 coordination sphere are presented in Table 2. For the three structural parameters, bigger Σ and smaller θ and ϕ imply larger geometric distortion of the FeN_6 coordination sphere. In the three series of structures, the degrees of distortion all follow the order of quintet > singlet. The $\text{Fe}-\text{N}_{\text{av}}$ lengths in different spin states are in line with the well-concluded experimental observation for Fe(II) SCO complexes.^{14,15} Generally, a length decrease of $\sim 0.2 \text{ \AA}$ occurs from the quintet to singlet state.

In addition, continuous shape measurements (CShMs) were used to identify the deviation of the coordination sphere to the

Table 2 Summary of some key structural parameters of the optimized structures 1–3 at different spin states

Complex	Spin state	Σ ($^\circ$)	θ ($^\circ$)	ϕ ($^\circ$)	Fe–N _{av} (\AA)	$S(O_h)$	$S(T_h)$
1	Singlet	91.38	89.17	178.52	1.962	2.16	9.50
1	Quintet	145.50	84.06	168.04	2.161	5.78	6.39
2	Singlet	88.18	88.22	179.61	1.962	2.14	9.53
2	Quintet	156.75	82.71	178.88	2.164	5.55	6.30
3	Singlet	91.55	89.98	179.92	1.967	2.28	9.26
3	Quintet	142.53	88.59	179.99	2.155	4.97	6.45

Σ : the sum of the deviations from 90° of the *cis* angles;³¹ θ : the dihedral angle between the planes of the pybox ligands;⁴ ϕ : the *trans*-N[pyridine]–Fe–N[pyridine] angle;⁴ Fe–N_{av}: the average value of the six Fe–N bond lengths in one FeN₆ coordination sphere; $S(O_h)$: the result of the CShM calculation denotes the deviation value of ideal O_h symmetry; $S(T_h)$: the result of the CShM calculation denotes the deviation value from ideal T_h after removing pyridine N.²⁷

ideal octahedron (O_h) and tetrahedron (T_d).²⁷ When the spin state is changed from the quintet to singlet state, significant decreases of the values of $S(O_h)$ and $S(T_d)$ are observed, suggesting that the symmetry increases from the high-spin to low-spin state. Overall, the structural parameters of six calculated structures quantitatively demonstrate the structural diversity in different ligand symmetries and spin states. The trend in the calculated structures is concomitant with the single crystal structures in specific spin states, also implying the reliability of the calculated results.

Based on the optimized structures of the three complexes in specific spin states ($S = 0$ and 2), their relative energies are presented in Fig. 5. Similar to other SCO systems,²⁸ the high-spin state of complex cations 1–3 with $S = 2$ is the ground state. The energy gaps between high spin ($S = 2$) and low spin ($S = 0$) for 1–3 are 14.90, 13.14, and 14.27 kJ mol^{−1}, respectively. Neese and co-worker have pointed out that the energy difference of 0 and 25.12 kJ mol^{−1} is proposed to be indicative of SCO behaviour.²⁹ The energy gaps of the three complexes are within this range in which the spin transitions are observed *via* magnetic measurements both in solution and in

the solid state. On comparison of relative energies for the three complexes, 3 possesses the lowest energies in both spin states. Conversely, the two states for 2 are the highest. The energy calculations disclose that the relative structural stability is in the order of $3 > 1 > 2$, consistent with the structural investigation for intramolecular steric congestion. The discrimination of stability between 2 and 3 was also confirmed by ¹H NMR experiments. When equimolar amounts of (*R*)-2(ClO₄) and (*S*)-2(ClO₄) were dissolved in acetonitrile, racemization was performed and the sole crystals of 3(ClO₄) were grown after vapor diffusion of ether into the solution (see Fig. S18†).³⁰ The energy gap between 2 and 3 in the quintet state is just 5.58 kJ mol^{−1}, which is small enough for the occurrence of racemization at ambient temperature. Additionally, the spin density maps of the three complex cations at quintet states were calculated, showing that the spin density is partially delocalized at the coordinated N atoms and pyridine ring (see Fig. S48†).

Solid-state magnetic studies

Subsequently, the temperature-dependent magnetic susceptibilities for four complexes constructed from the *meso* ligand, 1 (ClO₄), 1(BF₄)·MeCN, 1(PF₆)·MeCN, and 1(BPh₄)·MeCN·Et₂O, in the solid state were measured using SQUID. The effect of the counter anion and/or co-crystallized solvent in these complexes was disclosed.^{32–36} Because the rear three crystals were grown in the solvated form, they were protected with Parafilm to minimize solvent loss in the measurement of the first cycle. After completion of the first cycle, the samples were maintained at 400 K for 2 hours to completely remove the lattice solvent. Then the later cycles revealed the magnetic properties of desolvated samples. The temperature-dependent magnetic susceptibilities for the four complexes under successive cycles are shown in Fig. 6 and S43,† indicative of the variable SCO behaviour of *meso* type complexes as per the counter anion and co-crystallized solvent.

For 1(ClO₄), its $\chi_M T$ value at 300 K is only 0.64 cm³ K mol^{−1} and gradually decreases to zero at low temperature, indicating that most of the iron(II) ions are located at the low-spin state in the range of 2–300 K. Upon warming, the $\chi_M T$ value gradually increases to 2.05 cm³ K mol^{−1} at 400 K, but just reaching the high-spin population of ~53% (see Fig. 6(a), assuming that the

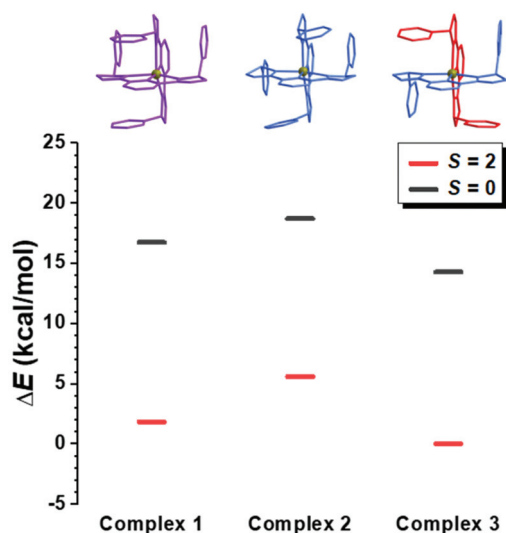


Fig. 5 Energy diagram for different spin multiplicities for the complex cations of 1, 2, and 3.

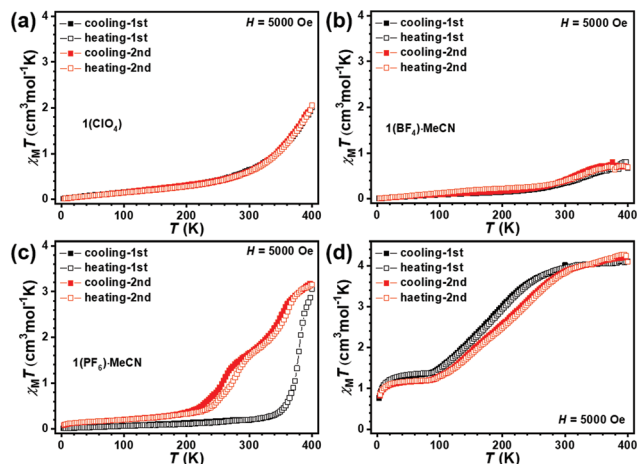


Fig. 6 Temperature dependence of $\chi_M T$ for $1(\text{ClO}_4)$ (a), $1(\text{BF}_4)\cdot\text{MeCN}$ (b), $1(\text{PF}_6)\cdot\text{MeCN}$ (c), and $1(\text{BPh}_4)\cdot\text{MeCN}\cdot\text{Et}_2\text{O}$ (d) upon two repeated scanings.

saturated $\chi_M T$ value at the complete HS state is $3.9 \text{ cm}^3 \text{ K mol}^{-1}$. $1(\text{BF}_4)\cdot\text{MeCN}$ also displays an incomplete SCO in the temperature range of 2–400 K. At 400 K, the $\chi_M T$ value only reaches $0.70 \text{ cm}^3 \text{ K mol}^{-1}$, far away from its complete HS state (see Fig. 6(b)). The SCO behaviour in $1(\text{PF}_6)\cdot\text{MeCN}$ can be switched *via* lattice acetonitrile. The solvated sample is a complete LS compound in the temperature range of 2–300 K (see the $\chi_M T$ vs. T curves in the first cooling/heating cycle). Upon heating from 300 K, its $\chi_M T$ value undergoes an abrupt increase to $3.06 \text{ cm}^3 \text{ K mol}^{-1}$ at 400 K as a result of the removal of the lattice solvent. Afterwards, the desolvated sample displays a two-step SCO behaviour (see Fig. 6(c)). The first transition at a higher temperature range shows no thermal hysteresis and its $T_{1/2}$ value is ~ 360 K. In the second SCO, a hysteresis loop of $\Delta T = 20$ K appears ($T_{1/2\downarrow} = 260$ K and $T_{1/2\uparrow} = 280$ K). This loop is stable and repeatable at the temperature-scan rate of 3 K min^{-1} (see Fig. S44[†]). The loss of the lattice solvent releases the crowd, thus reducing the geometric distortion of the Fe(II) complex cation, making the electron configuration favor the low-spin state. $1(\text{BPh}_4)\cdot\text{MeCN}\cdot\text{Et}_2\text{O}$ features an incomplete SCO. It locates in a complete high-spin state above 300 K. Upon cooling, the spin transition takes place and ends at ~ 72 K with a $\chi_M T$ value of $1.34 \text{ cm}^3 \text{ K mol}^{-1}$, indicative of the residual HS population of $\sim 34\%$. In the second cycle, desolvation results in the spin transition region moving to a high temperature of ~ 40 K (see Fig. 6(d)).

Moreover, the solvent effects in *optically pure* and *racemic* ligand type complexes were tested (see Fig. S45 and S46[†]). Two complexes with methanol as the lattice solvent were grown (see Fig. S27–S30[†]). Before and after the removal of lattice methanol, $2(\text{ClO}_4)\cdot\text{MeOH}$ displays a two-step SCO. The transitions of solvated and desolvated forms are both different compared with previously reported $2(\text{ClO}_4)\cdot\text{MeCN}$ (see Fig. S45[†]). It suggests that the annealing phases from two solvated complexes are different. Unlike $3(\text{ClO}_4)\cdot\text{MeCN}$ which is SCO-active both in solvated and desolvated forms, $3(\text{ClO}_4)\cdot\text{MeOH}$ remains

at the high-spin state regardless of the removal of the lattice solvent (see Fig. S46[†]). These results reveal that the structural symmetry, counter anion and lattice solvent jointly influence the spin-state behaviour of the complex in the solid state.³⁷

Magneto-structural correlation studies

Finally, the structural factors that can directly affect the spin-state behaviour are discussed. First, to reveal the unique effect by structural symmetry, we focus on the optimized calculated complex cations to compare their structural diversity caused by ligand symmetry. From the six optimized structures, it is found that the oxazoline rings exhibit considerable geometric distortion. To describe the degree of distortion quantitatively, a structural parameter μ_{rms} is introduced. This parameter is defined as the root mean square of the distances (μ , Å) of atoms in the oxazoline ring to the mean coordinated plane constructed by the central Fe(II) ion and three N atoms (shown in light green, see Fig. 7(a)). The μ_{rms} values of each structure are calculated from the projection distances of twenty atoms in four oxazoline rings to the coordination plane and are shown in Fig. 7(b) and Table S7.[†] 2 displays the largest deviation compared with 1 and 3 in two spin states. Conversely, the relative μ_{rms} values of 3 are the smallest. Additionally, 2 shows the largest variation in the μ_{rms} value between singlet and quintet states. According to the analyses of the data, two conclusions can be obtained: (1) the oxazoline rings in 2 show the largest geometric distortion in two states due to steric congestion^{38,39} and (2) the spin transition causes oxazoline rings in 2 to encounter the greatest structural change. Generally, large geometric distortion in coordination will weaken the ligand field and thus favor the high-spin state.^{40,41} The great structural change in high-spin and low-spin states makes the occurrence of SCO more difficult.⁴ The structural feature can well explain why 2 possesses the lowest $T_{1/2}$. A similar phenomenon is also observed in another structural parameter θ (see Fig. S49[†]). The angle θ is the dihedral angle between two ligand planes.⁴² Owing to the high symmetry of 3, a minor change in θ takes place during the SCO process. The correlation between single point energy and $T_{1/2}$ is plotted (see Fig. S50[†]), indicating that the structure of the lower energy level favours the low-spin state.

The structural features of the available single crystal structures of phenyl-substituted $[\text{Fe}(\text{pybox})_2]^{2+}$ are summarized and

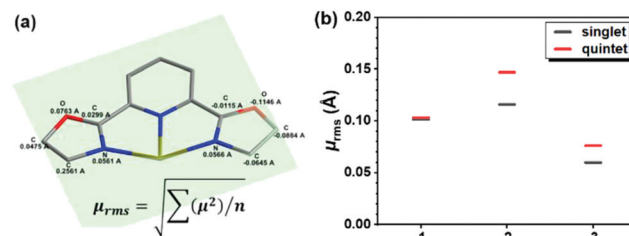


Fig. 7 (a) Definition and equation of the μ_{rms} value for the deviation of atoms in the oxazoline ring from coordination planarity; (b) the μ_{rms} values of three calculated structures in specific spin multiplicities.

compared. Except $1(\text{ClO}_4)$ which is in a desolvated form, all others contain lattice solvents. The co-crystallized solvents in the unit cell affect the packing of complex molecules. In most cases, they produced great geometric distortion in the solid state. After the loss of the solvent, SCO emerges or moves to a higher temperature. It is evident that the removal of the solvent results in the release of structural distortion of the complex cation. The lattice solvent, together with the steric congestion of adjacent phenyl rings and the counter anion, contributes to the twisting of the phenyl substituent. Normally, larger phenyl twisting can be observed in the *optically pure* and solvated compounds (see Tables S2–S5†).

Conclusions

In summary, we have investigated and compared the discrimination of structural symmetry and SCO behaviour in *optically pure*, *racemic*, and *meso* ligand type $[\text{Fe}(\text{pybox})_2]^{2+}$ isomers bearing phenyl substituents. The diverse orientations of the chiral centre in the ligand result in totally different molecular symmetries of the complexes. In this series of complexes, chiral discrimination has a great impact on their SCO behaviour both in solution and in the solid state. The ‘mismatched’ chiral arrangement produces steric congestion of phenyl substituents thereby distorting the FeN_6 coordination octahedron. DFT calculations give the energy profile of three type complexes in different spin multiplicities. The *racemic* type complex displays the highest symmetry and possesses relatively low energies in two multiplicities. According to the analyses of the optimized calculation structures, less geometric distortion in **3** is found. The high symmetry of coordination geometry imposes a higher ligand field and thus favours the low-spin state. It is consistent with the experimental investigation in acetonitrile that reports that $3(\text{ClO}_4)$ has the highest $T_{1/2}$ in this series. In the *meso* series complexes, SCO properties are also strongly affected by the counter cation and lattice solvent. This work systematically discusses the influence of ligand symmetry on the spin state and reveals that subtle structural discrimination in isomers can fine-tune the SCO behaviour.

Experimental

Synthesis of **1**

A solution of 2,6-pyridinedicarboxylic acid (8.35 g, 0.5 mol) and concentrated H_2SO_4 (1 mL) in methanol (50 mL) was heated under reflux for 3 hours. After cooling to ambient temperature, the solvent was removed under vacuum. The crude product was dissolved in ethyl acetate and washed with water (50 mL \times 3) and brine (50 mL) successively and dried over anhydrous sodium sulfate. After the solvent was removed under reduced pressure, the product was obtained as a white powder without the need for further purification (8.87 g, 91%).

Synthesis of **2**⁴³

A mixture of **1** (3.71 g, 19.03 mmol), (*S*)-2-amino-2-phenylethanol (2.35 g, 17.12 mmol) and MeOH (30 mL) was added to a sealed tube; then the mixture was stirred at 110 °C for 48 hours. After removing the solvent under vacuum, the crude product was purified by column chromatography (SiO_2 , petroleum ether/ethyl acetate, 1 : 2) to give compound **2** as a light yellow solid (3.07 g, 59%). ^1H NMR (600 MHz, CDCl_3): δ 9.12 (d, J = 7.3 Hz, 1H), 8.24 (dd, J_1 = 7.8 Hz, J_2 = 0.9 Hz, 1H), 8.20 (dd, J_1 = 7.8 Hz, J_2 = 1.0 Hz, 1H), 7.94 (t, J = 7.8 Hz, 1H), 7.42 (d, J = 7.4 Hz, 2H), 7.36 (t, J = 7.6 Hz, 2H), 7.29 (t, J = 7.3 Hz, 1H), 5.30 (dd, J_1 = 12.2 Hz, J_2 = 7.2 Hz, 1H), 4.08–4.05 (m, 2H), 4.04 (s, 3H), 3.40 (t, J = 6.2 Hz, 1H).

Synthesis of **3**

A mixture of **2** (3.05 g, 10.2 mmol), (*R*)-2-amino-2-phenylethanol (2.05 g, 14.9 mmol) and MeOH (20 mL) was added to a sealed tube; then the mixture was stirred at 110 °C for 48 hours. After removing the solvent under vacuum, the crude product was purified by column chromatography (SiO_2 , ethyl acetate) to give compound **3** as a white solid (3.44 g, 83%). ^1H NMR (400 MHz, $\text{DMSO}-d_6$): δ 9.31 (d, J = 9.0 Hz, 1H), 8.26–8.13 (m, 2H), 7.47 (d, J = 7.2 Hz, 2H), 7.35 (t, J = 7.4 Hz, 2H), 7.28 (t, J = 7.2 Hz, 1H), 5.20 (dd, J_1 = 14.5 Hz, J_2 = 6.7 Hz, 1H), 5.10 (t, J = 5.3 Hz, 1H), 3.83 (pd, J_1 = 11.3 Hz, J_2 = 7.1 Hz, 2H). ^{13}C NMR (151 MHz, DMSO): δ 163.3, 149.2, 140.8, 139.5, 128.3, 127.1, 127.0, 124.7, 64.5, 55.6. HRMS (MALDI-TOF) calcd for $\text{C}_{23}\text{H}_{23}\text{N}_3\text{O}_4$ $[\text{M} + \text{H}]^+$ 406.17, found 406.08. Anal. calcd for $\text{C}_{23}\text{H}_{23}\text{N}_3\text{O}_4$: C, 68.13; H, 5.72; N, 10.36. Found: C, 68.01; H, 5.62; N, 10.56.

Synthesis of **L**^{meso}

A solution of **3** (1.13 g, 2.8 mmol), TsCl (1.32 g, 6.8 mmol), DMAP (34 mg, 6.8 mmol) and Et_3N (2 mL) in CH_2Cl_2 was stirred at 0 °C for 3 hours. Subsequently, the mixture was heated to 110 °C for 48 hours. After cooling to ambient temperature, the solution was diluted with CH_2Cl_2 (10 mL) and washed with 1 N NaOH aqueous solution (10 mL), the organic phase was washed with DI water (30 mL \times 3) and brine (30 mL) and subsequently dried over anhydrous sodium sulfate. After the solvent was removed, the solid was washed with ethanol (10 mL) and then filtered to give **L**^{meso} as a white crystalline powder (560 mg, 53%). ^1H NMR (600 MHz, CDCl_3): δ 8.34 (d, J = 7.8 Hz, 2H), 7.92 (t, J = 7.8 Hz, 1H), 7.41–7.27 (m, 10H), 5.46 (t, J = 9.5 Hz, 2H), 4.97–4.90 (m, 2H), 4.43 (t, J = 8.6 Hz, 2H). ^{13}C NMR (151 MHz, CDCl_3): δ 165.1, 148.3, 143.3, 139.1, 130.5, 129.5, 128.4, 128.0, 79.0, 78.8, 78.6, 71.9. HRMS (MALDI-TOF) calcd for $\text{C}_{23}\text{H}_{19}\text{N}_3\text{O}_2$ $[\text{M} + \text{H}]^+$ 370.15, found 370.03. Anal. calcd for $\text{C}_{23}\text{H}_{19}\text{N}_3\text{O}_2$: C, 74.78; H, 5.18; N, 11.37. Found: C, 74.98; H, 5.23; N, 11.30.

Synthesis of **1(ClO₄)**

A solution of $\text{Fe}(\text{ClO}_4)_2 \cdot 6\text{H}_2\text{O}$ (36 mg, 0.1 mmol) in methanol (5 mL) was added to a stirred methanol solution (5 mL) of **L**^{meso} (74 mg, 0.2 mmol). The dark violet solution was stirred

for 30 minutes and concentrated under vacuum. Dark violet cubic crystals (73 mg, 74%) were obtained by slow diffusion of ether vapor into an acetonitrile solution of the complex. ^1H NMR (600 MHz, CD_3CN , 298 K): δ 55.30 (br, 2H), 53.54 (br, 2H), 25.55 (s, 2H), 12.32 (s, 2H), 10.43 (s, 2H), 9.21 (s, 2H), 7.91 (s, 2H), 7.62 (s, 4H), 6.59 (s, 4H), 6.23 (s, 6H), 4.11 (s, 2H), 3.23 (s, 4H), 2.44 (s, 4H). Anal. calcd for $\text{C}_{46}\text{H}_{38}\text{Cl}_2\text{FeN}_6\text{O}_{12}$: C, 55.61; H, 3.86; N, 8.46. Found: C, 55.21; H, 3.62; N, 8.79.

Synthesis of $1(\text{BF}_4)\text{-MeCN}$

The procedure is identical to that of $1(\text{ClO}_4)$ except that $\text{Fe}(\text{ClO}_4)_2\cdot 6\text{H}_2\text{O}$ was replaced by $\text{Fe}(\text{BF}_4)_2\cdot 6\text{H}_2\text{O}$. Dark purple cubic crystals (62 mg, yield: 64%) were obtained. ^1H NMR (600 MHz, CD_3CN , 298 K): δ 55.39 (br, 2H), 53.57 (br, 2H), 25.74 (s, 2H), 12.25 (s, 2H), 10.29 (s, 2H), 9.03 (s, 2H), 7.94 (s, 2H), 7.65 (s, 4H), 6.58 (s, 2H), 6.22 (s, 6H), 5.98 (br, 2H), 3.97 (s, 2H), 3.19 (s, 4H), 2.35 (s, 4H). Anal. calcd for $\text{C}_{48}\text{H}_{41}\text{B}_2\text{F}_8\text{FeN}_7\text{O}_4$: C, 57.12; H, 4.09; N, 9.71. Found: C, 56.91; H, 3.87; N, 9.39.

Synthesis of $1(\text{PF}_6)\text{-5MeCN}$

The procedure is identical to that of $1(\text{ClO}_4)$ except that $\text{Fe}(\text{ClO}_4)_2\cdot 6\text{H}_2\text{O}$ was replaced by $\text{FeCl}_2\cdot 4\text{H}_2\text{O}$ and KPF_6 . Dark purple cubic crystals (86 mg, yield: 79%) were obtained. ^1H NMR (600 MHz, CD_3CN): δ 55.81 (br, 2H), 54.00 (br, 2H), 25.88 (s, 2H), 12.37 (s, 2H), 10.31 (s, 2H), 9.07 (s, 2H), 7.94 (s, 2H), 7.65 (s, 4H), 6.58 (s, 2H), 6.22 (s, 6H), 5.97 (br, 2H), 3.95 (s, 2H), 3.13 (s, 4H), 2.32 (s, 4H). Anal. calcd for $\text{C}_{52}\text{H}_{47}\text{F}_{12}\text{FeN}_9\text{O}_4\text{P}_2$: C, 52.15; H, 4.14; N, 11.95. Found: C, 51.48; H, 3.66; N, 9.98.

Synthesis of $1(\text{BPh}_4)\text{-MeCN-Et}_2\text{O}$

The procedure is identical to that of $1(\text{ClO}_4)$ except that $\text{Fe}(\text{ClO}_4)_2\cdot 6\text{H}_2\text{O}$ was replaced by $\text{FeCl}_2\cdot 4\text{H}_2\text{O}$ and NaBPh_4 . Dark purple cubic crystals (110 mg, yield: 76%) were obtained. ^1H NMR (600 MHz, CD_3CN , 298 K): δ 56.01 (br, 2H), 54.19 (br, 2H), 25.89 (s, 2H), 12.44 (s, 2H), 10.29 (s, 2H), 9.05 (s, 2H), 7.94 (s, 2H), 7.63 (s, 4H), 7.34 (br, 16H), 7.03 (t, $J = 7.0$ Hz, 16H), 6.88 (t, $J = 7.0$ Hz, 8H), 6.58 (s, 2H), 6.22 (s, 2H), 5.98 (br, 2H), 3.97 (s, 2H), 3.07 (s, 4H), 2.30 (s, 4H). Anal. calcd for $\text{C}_{100}\text{H}_{91}\text{B}_2\text{FeN}_7\text{O}_5$: C, 77.57; H, 5.92; N, 6.33. Found: C, 77.98; H, 5.56; N, 6.87.

Synthesis of $2(\text{ClO}_4)\text{-MeOH}$

A solution of L^{S} (74 mg, 0.2 mmol) in methanol and CH_2Cl_2 (v/v, 10:1, 6 mL) was placed in the bottom of a test tube, methanol (10 mL) was gently layered on the top of the solution, and then a solution of $\text{Fe}(\text{ClO}_4)_2\cdot 6\text{H}_2\text{O}$ (36 mg, 0.1 mmol) in methanol (6 mL) was carefully added as the top layer. After a few weeks, dark red block crystals were collected (46 mg, 48%). ^1H NMR (600 MHz, CD_3CN , 298 K): δ 56.42 (br, 4H), 30.03 (br, 4H), 24.96 (s, 2H), 17.52 (s, 4H), 5.03 (s, 4H), 4.66 (s, 4H), 3.34 (s, 8H), -3.03 (s, 8H). Anal. calcd for $\text{C}_{47}\text{H}_{42}\text{Cl}_2\text{FeN}_6\text{O}_{13}$: C, 55.04; H, 4.13; N, 8.19. Found: C, 55.41; H, 3.92; N, 8.56.

Synthesis of $3(\text{ClO}_4)\text{-MeOH}$

The procedure is identical to that of $2(\text{ClO}_4)\text{-MeOH}$ except that L^{S} was replaced by equal amounts of L^{S} and L^{R} . Dark red block crystals were obtained with a yield of 57%. ^1H NMR (600 MHz, CD_3CN , 298 K): δ 40.83 (br, 4H), 21.35 (s, 2H), 7.48 (s, 4H), 7.22 (s, 4H), 6.86 (s, 8H), 6.18 (s, 4H), 4.52 (br, 4H), 3.43 (s, 8H). Anal. calcd for $\text{C}_{47}\text{H}_{42}\text{Cl}_2\text{FeN}_6\text{O}_{13}$: C, 55.04; H, 4.13; N, 8.19. Found: C, 55.35; H, 3.82; N, 8.51.

Synthesis of analogous Zn complexes

Three Zn(II) complexes, $[\text{Zn}(\text{L}^{\text{meso}})_2][\text{ClO}_4]_2$ ($1(\text{ClO}_4)\text{-Zn}$), $[\text{Zn}(\text{L}^{\text{R}})_2][\text{ClO}_4]_2$ ($2(\text{ClO}_4)\text{-Zn}$), and $[\text{Zn}(\text{L}^{\text{R}}\text{L}^{\text{S}})][\text{ClO}_4]_2$ ($3(\text{ClO}_4)\text{-Zn}$), were synthesized using a similar procedure to that of their archetypic Fe(II) complexes except that $\text{Zn}(\text{ClO}_4)_2$ was used as the metal source; the products were afforded as white powders after drying under vacuum. $1(\text{ClO}_4)\text{-Zn}$: ^1H NMR (600 MHz, CD_3CN , 298 K): δ 8.42 (t, $J = 7.9$ Hz, 2H), 8.32 (d, $J = 7.9$ Hz, 2H), 7.61 (d, $J = 7.9$ Hz, 2H), 7.18 (t, $J = 7.2$ Hz, 2H), 7.15–7.04 (m, 10H), 7.01 (t, $J = 7.7$ Hz, 4H), 6.65 (d, $J = 7.3$ Hz, 4H), 5.49–5.35 (m, 4H), 5.21 (t, $J = 7.4$ Hz, 2H), 4.91–4.77 (m, 2H), 4.54–4.42 (m, 4H). Anal. calcd for $\text{C}_{46}\text{H}_{38}\text{Cl}_2\text{ZnN}_6\text{O}_{12}$: C, 55.08; H, 3.82; N, 8.38. Found: C, 54.81; H, 4.01; N, 8.02. $2(\text{ClO}_4)\text{-Zn}$: ^1H NMR (600 MHz, CD_3CN , 298 K): δ 8.47 (t, $J = 7.9$ Hz, 2H), 8.04 (d, $J = 7.9$ Hz, 4H), 7.21 (t, $J = 7.4$ Hz, 4H), 7.08 (t, $J = 7.7$ Hz, 8H), 6.76 (d, $J = 7.3$ Hz, 8H), 5.26–5.20 (m, 4H), 5.17 (t, $J = 10.6$ Hz, 2H), 4.74 (dd, $J_1 = 10.7$ Hz, $J_2 = 8.8$ Hz, 2H). Anal. calcd for $\text{C}_{46}\text{H}_{38}\text{Cl}_2\text{ZnN}_6\text{O}_{12}$: C, 55.08; H, 3.82; N, 8.38. Found: C, 55.01; H, 3.99; N, 8.09. $3(\text{ClO}_4)\text{-Zn}$: ^1H NMR (600 MHz, CD_3CN , 298 K): δ 8.46 (t, $J = 7.9$ Hz, 2H), 7.99 (d, $J = 7.9$ Hz, 4H), 7.28 (t, $J = 7.4$ Hz, 4H), 7.15 (t, $J = 7.7$ Hz, 8H), 6.94 (d, $J = 7.2$ Hz, 8H), 4.99 (dd, $J_1 = 10.3$ Hz, $J_2 = 9.5$ Hz, 2H), 4.79 (t, $J = 9.2$ Hz, 4H), 4.73–4.66 (m, 4H). Anal. calcd for $\text{C}_{46}\text{H}_{38}\text{Cl}_2\text{ZnN}_6\text{O}_{12}$: C, 55.08; H, 3.82; N, 8.38. Found: C, 54.93; H, 4.15; N, 7.98.

Computational details

The structures of three $[\text{Fe}(\text{pybox})_2]^{2+}$ complex cations were fully optimized without restrictions using the M06 functional with a 6-31G(d) basis set in the gas phase. Tables S9–S14† list the Cartesian coordinates for complexes 1–3 in different spin states. All calculations were carried out using the Gaussian 09 software.

Caution! Although not encountered in our experiments, perchlorate salts in the presence of organic ligands are potentially explosive. Only a small amount of the materials should be prepared and handled with care.

Conflicts of interest

There are no conflicts to declare.

Acknowledgements

This work is partially supported by the National Natural Science Foundation of China (Grant No. 21771049, 21421005,

91422302, 21429201, 21871039 and 21801037), the State Key Laboratory of Fine Chemicals at Dalian University of Technology (KF 1607) and the Fundamental Research Funds for the Central Universities of China (Grant No PA2019GDPK0055 and PA2020GDJQ0028).

Notes and references

- P. Gütllich, A. B. Gaspar and Y. Garcia, *Beilstein J. Org. Chem.*, 2013, **9**, 342–391.
- M. A. Halcrow, *Spin-Crossover Materials: Properties and Applications*, John Wiley & Sons, Chichester, 2013.
- P. Gutlich and H. A. Goodwin, in *Spin Crossover in Transition Metal Compounds I*, ed. P. Gutlich and H. A. Goodwin, 2004, vol. 233, pp. 1–47.
- M. A. Halcrow, *Chem. Soc. Rev.*, 2011, **40**, 4119–4142.
- X.-P. Sun, Z. Tang, Z.-S. Yao and J. Tao, *Chem. Commun.*, 2020, **56**, 133–136.
- L. F. Qin, C. Y. Pang, W. K. Han, F. L. Zhang, L. Tian, Z. G. Gu, X. Ren and Z. Li, *Dalton Trans.*, 2016, **45**, 7340–7348.
- Y. Sekimoto, M. R. Karim, N. Saigo, R. Ohtani, M. Nakamura and S. Hayami, *Eur. J. Inorg. Chem.*, 2017, 1049–1053.
- J. Ru, F. Yu, P.-P. Shi, C.-Q. Jiao, C.-H. Li, R.-G. Xiong, T. Liu, M. Kurmoo and J.-L. Zuo, *Eur. J. Inorg. Chem.*, 2017, 3144–3149.
- H. A. Goodwin, in *Spin Crossover in Transition Metal Compounds I*, ed. P. Gutlich and H. A. Goodwin, 2004, vol. 233, pp. 59–90.
- Y.-Y. Zhu, C.-W. Liu, J. Yin, Z.-S. Meng, Q. Yang, J. Wang, T. Liu and S. Gao, *Dalton Trans.*, 2015, **44**, 20906–20912.
- Y.-Y. Zhu, H.-Q. Li, Z.-Y. Ding, X.-J. Lu, L. Zhao, Y.-S. Meng, T. Liu and S. Gao, *Inorg. Chem. Front.*, 2016, **3**, 1624–1636.
- Y. Pan, Y.-S. Meng, Q. Liu, W.-Q. Gao, C.-H. Liu, T. Liu and Y.-Y. Zhu, *Inorg. Chem.*, 2020, **59**, 7398–7407.
- A. Kimura and T. Ishida, *Inorganics*, 2017, **5**, 52.
- K. E. Burrows, S. E. McGrath, R. Kulmaczewski, O. Cespedes, S. A. Barrett and M. A. Halcrow, *Chem. – Eur. J.*, 2017, **23**, 9067–9075.
- W.-Q. Gao, Y.-S. Meng, C.-H. Liu, Y. Pan, T. Liu and Y.-Y. Zhu, *Dalton Trans.*, 2019, **48**, 6323–6327.
- Z. Y. Li, H. Ohtsu, T. Kojima, J. W. Dai, T. Yoshida, B. K. Breedlove, W. X. Zhang, H. Iguchi, O. Sato, M. Kawano and M. Yamashita, *Angew. Chem., Int. Ed.*, 2016, **55**, 5184–5189.
- K. E. Burrows, R. Kulmaczewski, O. Cespedes, S. A. Barrett and M. A. Halcrow, *Polyhedron*, 2018, **149**, 134–141.
- L. J. Kershaw Cook, R. Kulmaczewski, R. Mohammed, S. Dudley, S. A. Barrett, M. A. Little, R. J. Deeth and M. A. Halcrow, *Angew. Chem., Int. Ed.*, 2016, **55**, 4327–4331.
- S. Rodriguez-Jimenez, M. Yang, I. Stewart, A. L. Garden and S. Brooker, *J. Am. Chem. Soc.*, 2017, **139**, 18392–18396.
- M. P. Shores, C. M. Klug and S. R. Fiedler, in *Spin-state switching in solution. Spin-Crossover Materials: Properties and Applications*, John Wiley & Sons Ltd, Chichester, 2013, pp. 281–301.
- D. F. Evans, *J. Chem. Soc.*, 1959, 2003–2005.
- C. Piguet, *J. Chem. Educ.*, 1997, **74**, 815.
- S. Rodriguez-Jimenez and S. Brooker, *Inorg. Chem.*, 2017, **56**, 13697–13708.
- S. Rodriguez-Jimenez, A. S. Barltrop, N. G. White, H. L. C. Feltham and S. Brooker, *Inorg. Chem.*, 2018, **57**, 6266–6282.
- M. J. Frisch, G. W. Trucks, H. B. Schlegel, G. E. Scuseria, M. A. Robb, J. R. Cheeseman, G. Scalmani, V. Barone, B. Mennucci, G. A. Petersson, H. Nakatsuji, M. Caricato, X. Li, H. P. Hratchian, A. F. Izmaylov, J. Bloino, G. Zheng, J. L. Sonnenberg, M. Hada, M. Ehara, K. Toyota, R. Fukuda, J. Hasegawa, M. Ishida, T. Nakajima, Y. Honda, O. Kitao, H. Nakai, T. Vreven, J. A. Montgomery Jr., J. E. Peralta, F. Ogliaro, M. Bearpark, J. J. Heyd, E. Brothers, K. N. Kudin, V. N. Staroverov, R. Kobayashi, J. Normand, K. Raghavachari, A. Rendell, J. C. Burant, S. S. Iyengar, J. Tomasi, M. Cossi, N. Rega, J. M. Millam, M. Klene, J. E. Knox, J. B. Cross, V. Bakken, C. Adamo, J. Jaramillo, R. Gomperts, R. E. Stratmann, O. Yazyev, A. J. Austin, R. Cammi, C. Pomelli, J. W. Ochterski, R. L. Martin, K. Morokuma, V. G. Zakrzewski, G. A. Voth, P. Salvador, J. J. Dannenberg, S. Dapprich, A. D. Daniels, O. Farkas, J. B. Foresman, J. V. Ortiz, J. Cioslowski and D. J. Fox, *GAUSSIAN 09, Revision E.01*, Gaussian, Inc., Wallingford, CT, 2009.
- Y. Zhao and D. G. Truhlar, *Theor. Chem. Acc.*, 2008, **120**, 215–241.
- M. Llunell, D. Casanova, J. Cirera, P. Alemany and S. Alvarez, *SHAPE, version 2.0*, Universitat de Barcelona, Barcelona, Spain, 2010.
- B. Dey, A. Mondal and S. Konar, *Chem. – Asian J.*, 2020, **15**, 1709–1721.
- S. Ye and F. Neese, *Inorg. Chem.*, 2010, **49**, 772–774.
- T.-T. Ma, X.-P. Sun, Z.-S. Yao and J. Tao, *Inorg. Chem. Front.*, 2020, **7**, 1196–1204.
- P. Guionneau, M. Marchivie, G. Bravic, J. F. Létard and D. Chasseau, *Top. Curr. Chem.*, 2004, **234**, 785–786.
- F. Kobayashi, Y. Komatsumaru, R. Akiyoshi, M. Nakamura, Y. Zhang, L. F. Lindoy and S. Hayami, *Inorg. Chem.*, 2020, **59**, 16843–16852.
- X. H. Zhao, S. L. Zhang, D. Shao and X. Y. Wang, *Inorg. Chem.*, 2015, **54**, 7857–7867.
- D. Shao, L. Shi, F. X. Shen, X. Q. Wei, O. Sato and X. Y. Wang, *Inorg. Chem.*, 2019, **58**, 11589–11598.
- C. Rajadurai, Z. Qu, O. Fuhr, B. Gopalan, R. Kruk, M. Ghafari and M. Ruben, *Dalton Trans.*, 2007, 3531–3537.
- M. Nihei, L. Han and H. Oshio, *J. Am. Chem. Soc.*, 2007, **129**, 5312–5313.
- X. P. Sun, R. J. Wei, Z. S. Yao and J. Tao, *Cryst. Growth Des.*, 2018, **18**, 6853–6862.
- I. Prat, A. Company, T. Corona, T. Parella, X. Ribas and M. Costas, *Inorg. Chem.*, 2013, **52**, 9229–9244.

- 39 R. Kulmaczewski, F. Bamiduro, N. Shahid, O. Cespedes and M. A. Halcrow, *Chem. – Eur. J.*, 2021, **27**, 2082–2092.
- 40 S. Q. Su, S. Q. Wu, M. L. Baker, P. Bencok, N. Azuma, Y. Miyazaki, M. Nakano, S. Kang, Y. Shiota, K. Yoshizawa, S. Kanegawa and O. Sato, *J. Am. Chem. Soc.*, 2020, **142**, 11434–11441.
- 41 S.-G. Wu, M. N. Hoque, J.-Y. Zheng, G.-Z. Huang, N. V. Ha Anh, L. Ungur, W.-X. Zhang, Z.-P. Ni and M.-L. Tong, *CCS Chem.*, 2020, 453–459.
- 42 M. A. Halcrow, I. Capel Berdiell, C. M. Pask and R. Kulmaczewski, *Inorg. Chem.*, 2019, **58**, 9811–9821.
- 43 P. Drabina, P. Funk, A. Růžička, J. Hanusek and M. Sedlák, *Transition Met. Chem.*, 2010, **35**, 363–371.